Thickness Measurement by Model-Based Exhaustive Analysis in Far-Infrared

Morgan Fouque, Nicolas Sutton-Charani, Olivier Strauss

Version of Record: https://www.sciencedirect.com/science/article/pii/S1350449521001146
Manuscript_a9108b3a192552fc610e7435dbf6fa63

Thickness Measurement by Model-Based Exhaustive Analysis in Far-Infrared

M. Fouque, N. Sutton-Charani and O.Strauss *†‡

March 30, 2021

Abstract

We propose a method for reconstructing the thickness variation of one layer of interest inside a multi-layered structure. This reconstruction is based on inverting far-infrared reflection measurements at a few distinct frequencies. This real-time method allows non-destructive evaluation of a multi-layered structure to better control its manufacturing process, whereas other methods have acquisition or computation times that are not compatible with real-time non-destructive evaluation. Two simulated data and one real data based experiments revealed that the method we propose is robust against measurement noise.

1 Introduction

Inspection is an essential aspect of the multilayered structure (MLS) creation process to address modern challenges. When using this type of structure the thickness of each of its layers has to be closely controlled during its manufacturing. Such structures have many applications. For example, in the aerospace sector, heat shields are multilayered. If one of the layers in this functional MLS is too thin or too thick, it could compromise the isolation property of other layers. Non-destructive evaluation (NDE) of such structures helps to better control their manufacturing process. This has a positive impact on both profitability and ecology.

This paper presents a fast convenient solution for inspecting one layer of an MLS when its computer-aided design (CAD) model is known.

By analogy to X-ray imaging, which provides images of material absorption, no technologies are available for qualitative and quantitative imaging of polymer

*This paragraph of the first footnote will contain the date on which you submitted your paper for review. This work was supported in part by the French ANRT under Grant 2018/0805.

†M. Fouque and O. Strauss are with the Laboratoire d'Informatique, Robotique et Microélectronique de Montpellier (LIRMM), Montpellier, France (e-mails: mfouque@lirmm.fr (corresponding author), strauss@lirmm.fr).

‡N. Sutton-Charani works at EuroMov Digital Health in Motion, Univ Montpellier, IMT Mines Alès, Alès, France (e-mail: nicolas.sutton-charani@mines-ales.fr).

and ceramic type materials, i.e X-rays are not sensitive enough to the absorption of such materials. Furthermore, NDE of complex structures usually requires a reflective setup (sensor and source on the same side of the sample), thus limiting the technological solutions for such a task. Far-infrared wavelengths have been shown to be effective in imaging such materials in a reflection setup but only with a qualitative approach. Perturbations occur in the far-infrared reflection images, known as Fabry-Pérot interference [1] [2], which complicate unsupervised evaluation (e.g detection of structural defects are only possible via expert assessment).

Physical modelling of those perturbations is however possible by using Maxwell's equations. Comparisons between theoretical models and actual observations through multiple frequencies are common in time-domain spectroscopy (TDS) and frequency-modulated continuous-wave (FMCW) approaches [3, 4]. Nevertheless, the broad range of frequencies used by TDS and FMCW systems requires high sweep acquisition times compared to fixed-frequency imaging. Therefore, simply using several frequencies could be a trade-off solution to generate accurate results in reasonable time, as implemented in the genetic and evolutionary material parameter reconstruction field [5, 6, 7, 8]. In these latter studies, the authors solved the inverse problem by giving hints about the parameters or using adaptative learning algorithms. Here we propose to compensate for the lack of information caused by the frequency restriction, which decreases the precision of quantitative measurements, by using optimum analysis and spatial regularisation rules.

The rest of the paper is divided as follows. Section 2 presents some of the most recent work on NDE applied to MLS thickness measurement, including recent far-infrared solutions. In Section 3, we discuss the difficulty of measuring thickness variations in a layer by using far-infrared due to the multivocity of this measurement. The solution we propose is based on modelling an MLS reflective response to a far-infrared beam. This modelling is given in Section 4. Section 5 presents our proposed solutions. Section 6 presents, through experiments, the thickness map reconstruction of two simulated and one real MLS. This highlights the properties of the solutions we propose for different noise levels. In section 7 we present our conclusions

2 Related work

NDE of complex MLS has been a major research focus in recent decades and has been approached in two different ways. The first is the classification solution, i.e. detecting whether or not the fabricated structure complies with an initial set of constraints. The second is the measurement solution, whereby a map of at least one MLS parameter variation is created. This article focuses on this second approach and involves creating a map of the thickness of a layer of interest (LoI).

Different technologies have been proposed in the relevant literature to obtain such a map: ultrasound [9], eddy currents [10], X-ray fluorescence [11], optical

coherence tomography [12], and photothermal methods [13]. For a complete overview of MLS NDE technologies see [14].

Each of these methods has caveats, as explained by J. Jonuscheit [15]: *They can either not resolve multilayer coatings (such as the eddy current and photothermal methods), or they penetrate relevant materials insufficiently (such as optical coherence tomography), or the process involves contact (such as ultrasound measuring technology). Only X-ray fluorescence could be used in this case, even though it is often unavailable due to radiation protection problems.* Far-infrared technology is a promising candidate to address this measurement problem. Far-infrared can penetrate through most non-conductive materials, accounting for a vast majority of MLS.

Far-infrared technologies have achieved multiple great results in addressing this problem [16, 17, 18, 19, 20, 21]. In [3], Ellrich et al. proposed an application of FMCW heterodyne measurement and TDS systems to deal with the thickness measurement problem. In [4], Schreiner et al. attempted thickness measurement using FMCW data with a brute-force comparison to theoretical data, thus effectively overcoming the Rayleigh resolution limit. However, both TDS and FMCW based solutions are time-consuming since both systems must sweep through an entire frequency band to acquire observations. In [5], Zwick et al. compared simulation and observation in a reflective setup of a sample at discrete frequencies or discrete observation angles. They retrieved material parameters for all layers of an observed MLS via genetic algorithm optimisation when the number of layers composing that MLS and their respective thicknesses were known. This method, in contrast to TDS or FMCW systems, could generate real-time observations. However, real time assessment is hampered by the use of genetic algorithms which are known to converge slowly and require tuning of multiple hyperparameters. The research of Zwick et al. has been followed by studies by numerous authors using genetic or evolutionary algorithms and artificial neural networks to retrieve material parameters [6, 7, 8]. In addition to the fact that these methods cannot be used for real-time imaging, they also dedicated to single-location assessment, not to complete MLS assessment.

Far-infrared active imaging allows real-time studies of samples at given frequencies and at multiple locations [22, 23, 24]. However, the obtained images (2D matrices of reflection or transmission measurements) do not allow precise visual assessment since Fabry-Pérot interference occurs which impedes conventional image processing techniques.

Fabry-Pérot interference has been studied by numerous authors. In [1], Costa et al. used a basic C-scan setup and showed that this interference happens because of the aggregation of the different responses of the materials with the cavities in the optical system itself. Lin et al. propose in [2] to take those effects into account with a frequency-domain spectrometer using acquisition paths of different lengths, thereby enhancing the material parameter measurement precision. In [25], Wang et al. showed that controlled phase unwrapping in low-loss media disambiguates the problem when phase information is available.

The solution we propose in this paper takes advantage of far-infrared imaging and allows real-time data processing. The methodology is similar to that of [4]

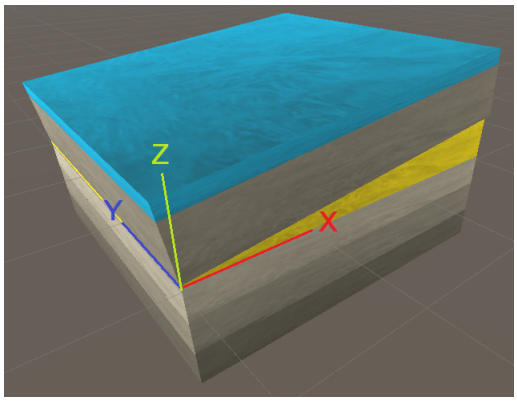

Figure 1: 3D Visualisation of a multi layered structure (MLS).

and [5] but only a few frequencies are used, exploiting the speed of active imaging systems and using the phenomenology causing the perturbations, as studied in [1] and [2], at different sampled locations to create a precise measurement map of a layer of interest's thickness variations within a multilayered structure.

3 Proposed setup

The goal of our study was to estimate a thickness map of a layer of interest (LoI). The reconstruction of this map is based on measuring the reflection response of the MLS at N x M regularly spaced locations. Those measurements are obtained by emitting a far-infrared beam at fixed frequencies at a particular location, focusing the beam on the sample at normal incidence and measuring the reflected electromagnetic field. Let I be the far-infrared reflection image collecting these measurements. $I(i,j)$ is the reflective response at location (x_i, y_j), $i = 1 \dots N$, $j = 1 \dots M$ for a particular wavelength λ.

Fig.1 shows a representative view of the CAD model of an MLS sample. Fig.2 shows a slice of that model in the (z,x) plane, at position $y = y_0$. The yellow layer (layer 3) is the LoI.

Let $\tau(x,y)$ be the thickness of the LoI at position (x,y) of the MLS to be inspected.

Fig.3 shows a far-infrared reflection image at 284 GHz of a silicone wedge linearly growing in thickness from 0.4 mm on the left to 1.5 mm on the right, between two polycarbonate (PC) slabs. Looking at the two highlighted area, we note that two different thicknesses exhibit the same reflective response. Finding thickness from measurement is therefore an ill-posed problem and must be solved by combining multiple sources of information.

A way to increase the information is to acquire f different far-infrared reflection images $I_1 \dots I_f$ associated with f different wavelengths $\lambda_1 \dots \lambda_f$. If the wavelengths are suitably chosen, then for each (i,j) the f equations $I_n(i,j) = \mathcal{M}(z, \lambda_n)$ $(n = 1 \dots f)$ have a single solution $\hat{z}(i,j) = \tau(x_i, y_j)$, with $\mathcal{M}(z, \lambda_n)$

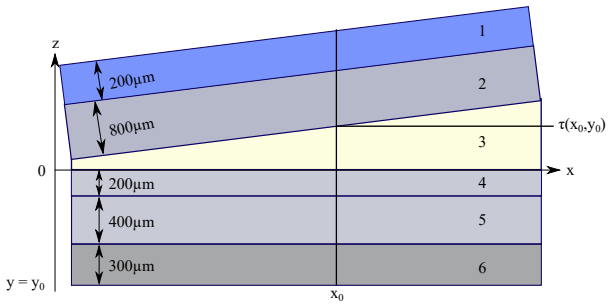

Figure 2: A slice of the MLS represented in Fig.1.

being a function that models the reflection response of a theoretical object representing our real object at position (x_i, y_j) with an LoI measuring z mm at wavelength λ_n.

4 MLS Modelling

We propose to model the MLS to be inspected as a stack of L semi-infinite layers, characterised by their thickness and their complex refractive index, as shown in Fig.2. The decrease in the speed of light in the material is characterised by the real part of the refractive index and the extinction coefficient by it's imaginary part.

Different methods can be used to simulate the reflective response of this structure when exposed to far-infrared light, such as finite-dimension time-domain simulations, finite-element methods, method of moments, etc. In this study, since we aimed at achieving a real-time solution, we used the one dimensional propagation method similar to the Rouard method described in S.J Orfanidis's book ([26]). This modelling was chosen because it just involves a few simple operations.

Let us suppose that the assessed MLS is made of L homogeneous dielectric layers. Each layer has a complex refractive index n_l ($l = 1 \dots L$) and a thickness t_l. The structure exists between two semi-infinite media having a refractive index of n_0 and n_{L+1}. Let us suppose that the LoI is the K^{th} layer. Its thickness is unknown but its refractive index is known. Let $\rho_l = \frac{n_{l-1}-n_l}{n_{l-1}+n_l}$ be the Fresnel reflection coefficient at interface l ($l = 1 \dots L+1$). Computation of the reflective response of this structure to far-infrared radiation of wavelength λ in free space at location (x, y) can be obtained by the following backward recursion (see [26]):

$$\Gamma_{L+1} = \rho_{L+1},$$
$$\Gamma_l = \frac{\rho_l + \Gamma_{l+1} e^{-j(4\pi n_l t_l)/\lambda}}{1 + \rho_l \Gamma_{l+1} e^{-j(4\pi n_l t_l)/\lambda}},$$
$$(l = L \dots 1),$$

This method enables us to model the reflective response function $\mathcal{M}$ at any location (x, y) of the MLS by: $\mathcal{M}(\tau(x, y), \lambda) = \Gamma_1$, supposing that the thickness of the LoI at location (x, y) equals $\tau(x, y)$. Finding $\tau(x_i, y_j)$ amounts to finding the value $\hat{z}(i, j)$ such that $I_n(i, j) = \mathcal{M}(\hat{z}(i, j), \lambda_n)$ for $n = 1 \dots f$.

5 Proposed method

For clarity, we propose to illustrate our method with a simulated MLS made of two 2.15mm PC slabs, with a silicone-type material sandwiched in-between. The silicone layer is linearly tapered from 0mm on the left of the sample to 3mm on the right. This is a particular case of the MLS presented in section 4 with L = 3, and K = 2 and the silicone layer being the LoI.

5.1 Direct solution

We first consider estimating the thickness of the LoI at each measurement point. Let us suppose that the thickness at location (x_i, y_j) is known to belong to an interval (a, b). Let us divide this interval into P values z_k $(k = 1 \dots P)$.

The method we propose is based on computing the quadratic difference between the f real measurements $\{I_n(i, j)\}_{n=1\dots f}$ at location (x_i, y_j) obtained for f different wavelengths $\{\lambda_n\}_{n=1\dots f}$ and the theoretical values $\{\mathcal{M}(z_k, \lambda_n)\}_{n=1\dots f}$ obtained by using a function $\mathcal{M}$ that models the reflection response of the MLS based on its CAD model:

$$Q_{i,j}(z_k) = \frac{1}{f} \sum_{n=1}^{f} (I_n(i, j) - \mathcal{M}(z_k, \lambda_n))^2$$

As $Q_{i,j}(z_k)$ decreases, the probability that the value z_k is the thickness of the LoI at location (x_i, y_j) increases. Naturally, using multiple frequencies (i.e. the higher f) increases the strength of this function by lowering the probability of finding wrong solutions. However, the acquisition system we used did not allow for real-time acquisition at more than 3 fixed-frequencies. We thus set $f \leq 3$. Fig.6 illustrates the strength of this function, for $f = 1 \dots 3$, by computing $Q_{i,j}(z_k)$ for the central point $(\frac{N}{2}, \frac{M}{2})$ of the proposed sample. In this experiment, $\tau(x_i, y_j) = 1.5$ mm, $a = 0$ mm and $b = 3$ mm. For $f = 1$, the multivaluedness of the solution is high, i.e. the quadratic error crosses zero at several locations, but low for $f = 2$, with only one location (1.5 mm) crossing zero but a few

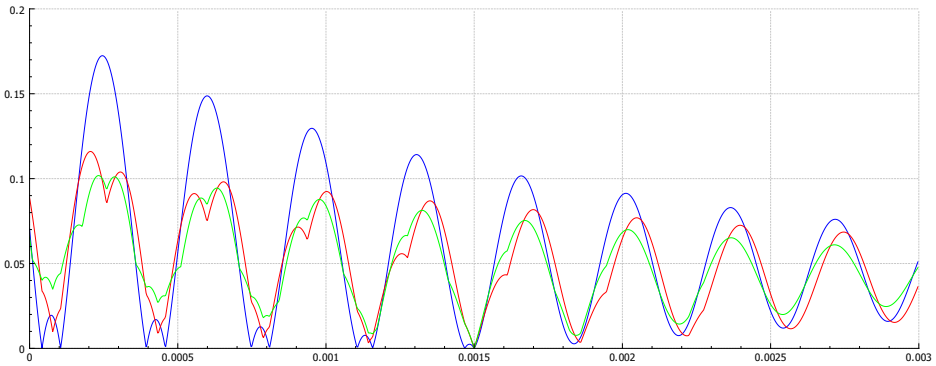

Figure 6: Plot of the mean quadratic difference with f = 1(blue), 2(red), 3(green).

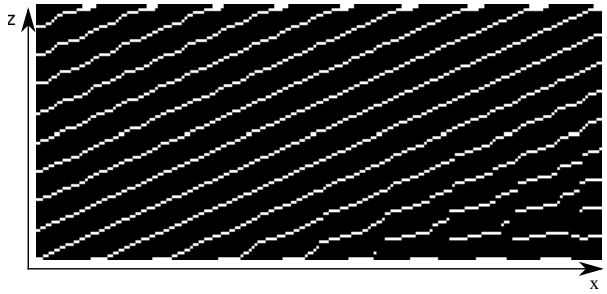

Figure 7: An (x, z)–slice of the local minima of $Q_{i,j}(z_k)$ when considering the proposed three-layered MLS. Local minima are represented in white.

other very close to zero, and 1.5 mm clearly seems to be the solution for $f = 3$. Hereafter we assume, without any loss of generality, that $\lambda_1 < \lambda_2 < \lambda_3$.

Thus the direct solution to this problem would consist of computing $\hat{z}(i, j)$ at each location (x_i, y_j), representing the global minimum of $Q_{i,j}(z_k)$, the Euclidean distance between the measurements and the model: $\hat{z}(i, j) = \underset{k=1,\ldots,P}{\arg\min}\{Q_{i,j}(z_k)\}$.

However, computing this solution could lead to unstable solutions due to discretisation of the $[a, b]$ interval in P samples.

5.2 Regularisation by connectivity

The direct solution is not stable enough to be used without regularisation. This instability is due to discretisation of the solution space w.r.t. the continuous nature of the problem to be solved. In addition, measurement noise could transform a local minimum into a global minimum.

The regularisation by connectivity we propose is based on the hypothesis that the thickness variation of the LoI is continuous, i.e. this function cannot have any sharp changes. This would not be true if this layer were broken, but

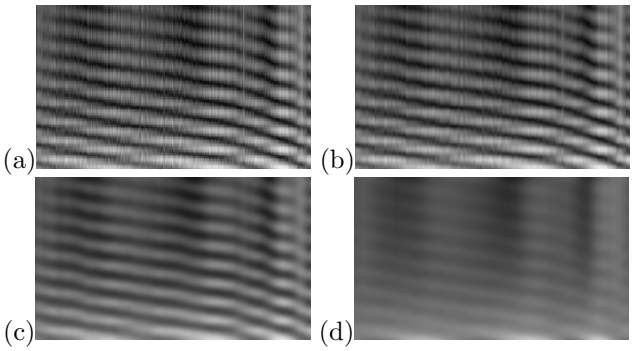

Figure 8: (a) Original projection of $Q_{i,j}(z_k)$. (b) Mean with a range of 3. (c) Mean with a range of 6. (d) Mean with a range of 12.

an assessment of this situation would be beyond the scope of this study.

The *regularisation by connectivity* we propose involves two steps.

The first step consists of finding, for each (i, j) location of the image plane, any value that is a local minimum of the quadratic function $Q_{i,j}$. A value z is said to be a local minimum if it is a global minimum of the quadratic function in the interval $[z - \epsilon, z + \epsilon]$, where ϵ equals half of the smallest quarter effective wavelength with respect to the LoI complex refractive index. We thus obtain a discrete set of local minima, as represented in Fig.7.

As can be seen in this Figure, the local minima define discrete planes of connected points. We say that two local minima are connected if they are associated with two connected pixels and if their distance (in z-value) is lower than ϵ. For each set of connected minima, we can compute the mean of the quadratic function of its elements.

The second step of the method consists of finding the set of connected minima that minimises the average quadratic error of its elements. This set is retained for representing the thickness surface of the LoI.

At this stage, there can be some measurement locations with no thickness estimate. This occurs when the reflection measurements are affected by noise that is strong enough to offset the z_k array by more than ϵ. In that case, we can interpolate the current solution. For a complete description of the mathematical process underlying this first regularisation, see Appendix A.

5.3 Regularisation by smoothing the quadratic function

As stated previously, computation of $Q_{i,j}(z_k)$ is sensitive to noise. Noise can come from the far-infrared sensors and sources, or from any external source not accounted for, such as room temperature and electromagnetic perturbations in the acquisition process. Excessive noise may break the thickness continuity we described in section 5.2 by offsetting the minima locations. Therefore the method only works in low-noise environments and requires additional processing to be noise-resilient.

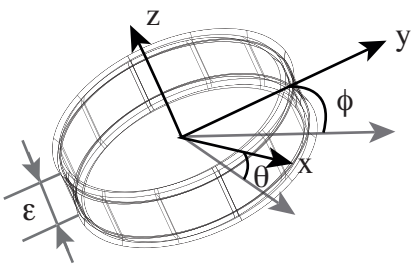

Figure 9: The non isotropic neighbourhood $\mathcal{V}_{\theta,\phi}(i,j,k)$ with orientation θ, ϕ

A common way to be noise resilient is to smooth the analysed function (here $Q_{i,j}(z_k)$). The simplest treatment to get a smoother discrete function is to replace each value $Q_{i,j}(z_k)$ by a value $\hat{Q}_{i,j}(z_k)$ obtained by averaging the original function in a discrete neighbourhood of each location (i,j,k). Note that the smoothing improves as the neighbourhood widens.

Fig.8a shows the projection of $Q_{i,j}(z_k)$ on the xz plane, in which there are many locations where noise would hamper the methodology proposed in Section 5.2 (note that every projection shown in this section was square rooted after the applied treatments for visualisation purposes, real valued square root preserving numerical order). Fig.8b shows a smoothed image with an averaging range of 3 pixels (i.e. averaging in a $[-3;+3]$ cube around i,j,k). In that case, the range is too short to provide significant effects. In Fig.8c, smoothing is performed by averaging in a range of 6 pixels. In that case, smoothing is sufficient to identify the thickness slopes we seek but some bridges between solutions start to appear. In Fig.8d, averaging was achieved with a range of 12 pixels. The thickness slopes almost disappear in this case. The stronger the smoothing, the more likely it is to see the information on the LoI thickness slope disappear, thus rendering Method 5.2 inoperable when strong smoothing is needed (strong noise).

We suggest offsetting the loss of information due to strong smoothing by using a non-isotropic neighbourhood whose orientation in each (i,j,k) location will depend on the thickness slope recovered. The neighbourhood we are proposing has a cylindrical shape with thickness ϵ, thereby allowing information to be collected with a precision at effective quarter wavelength precision. The smoothing improves as the cylinder diameter increases.

Let θ and ϕ be respectively the orientation of this cylinder in the x and y orientation. $\mathcal{V}_{\theta,\phi}(i,j,k)$ denotes the non-isotropic neighbourhood, with orientation θ, ϕ at location (i,j,k) (see Fig. 9).

For this non-isotropic neighbourhood to achieve smoothing in the direction of the slope, the appropriate angles $\hat{\theta}$ and $\hat{\phi}$ may be found at each location (i,j,k). By construction, these angles appear to be the angles that minimise the mean quadratic function inside the considered neighbourhood:

$$\hat{\theta}, \hat{\phi} = \arg\min_{\theta,\phi}\left(\frac{1}{|\mathcal{V}_{\theta,\phi}(i,j,k)|}\sum_{(i',j',k')\in\mathcal{V}_{\theta,\phi}(i,j,k)}(Q_{(i',j')}(z_{k'}))\right),$$

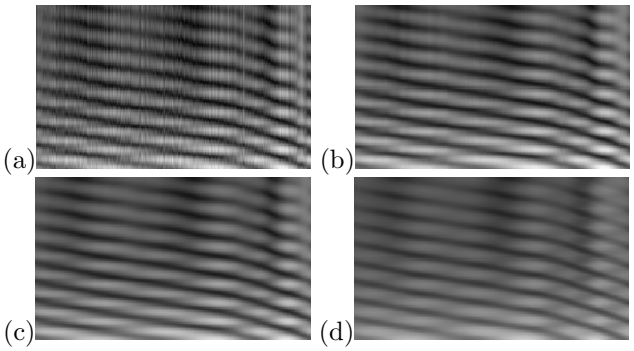

Figure 10: (a) Original projection of $Q_{i,j}(z_k)$. (b) Method 5.3 with a range of 3. (c) Method 5.3 with a range of 6. (d) Method 5.3 with a range of 12.

where $\theta, \phi \in [0, \frac{\pi}{2}]^2$ and $|\mathcal{V}_{\theta,\phi}(i,j,k)|$ is the cardinal of the considered neighbourhood.

The smoothed quadratic function $\hat{Q}$ is now expressed as:

$$\hat{Q}_{(i,j)}(z_k) = \frac{1}{|\mathcal{V}_{\theta,\phi}(i,j,k)|} \sum_{(i',j',k') \in \mathcal{V}_{\theta,\phi}(i,j,k)} (Q_{(i',j')}(z_{k'})).$$

Let us compare the results obtained by using isotropic smoothing (see Fig.8) with those obtained by using the proposed non-isotropic smoothing (see Fig.10). When comparing Fig.8c and Fig.10.d, non-isotropic smoothing with a range of 12 leads to a loss in information comparable to that of isotropic smoothing with a range of 6. Smoothing with a non-isotropic neighbourhood allows stronger smoothing with less information loss. Thus, replacing Q by $\hat{Q}$ in the regularisation by connectivity explained in section 5.2 improves its resilience to noise.

Note that, in practice, the operations presented are highly parallelisable and can therefore be calculated with GPUs.

6 Experiments

6.1 Experimental setup

The experimental setup we considered is the three-layered structure presented in Section 5[1] composed of two layers of 2.15 mm PC of complex refractive index $1.625 + 0.0019j$ and a central layer of silicone with a complex refractive index of $1.55 + 0.041j$. The refractive indices of both PC and silicone were measured with a TDS system. Our operating frequencies were $f_1 = 279$ GHz, $f_2 = 284$ GHz and $f_3 = 289$ GHz.

The acquisition system we used consisted of a far-infrared source, based on broadband Schottky diode multiplier chains emitting continuous waves in

[1] see also Fig.1, 2, with only one layer above and below the yellow layer.

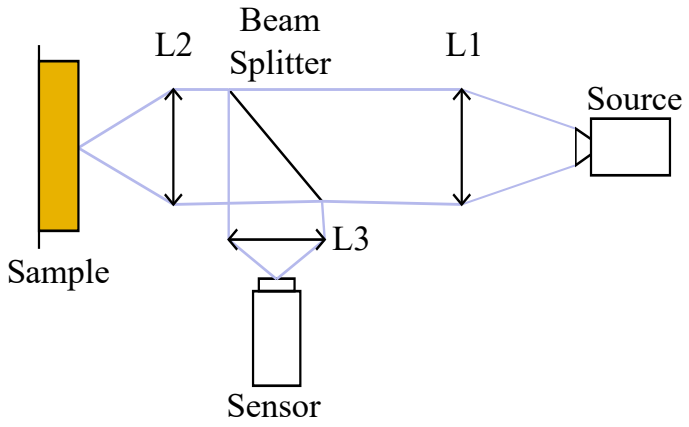

Figure 11: Acquisition system used for the real experiment.

the 220-330 GHz bandwidth guided through lenses, focused on the sample and reflected toward a Schottky diode sensor via a beam splitter, as presented in Fig.11. L1 is a collimation lens while L2 and L3 are focusing lenses of 100 mm focal length. The MLS under inspection is then scanned on the x and y axes with translation stages.

Three experiments were carried out, two simulation experiments and a real experiment. In the simulation experiments, as illustrated in Fig. 2, the thickness of the silicone layer varied linearly from 0 mm to 3 mm. In the real experiment, it was not possible to monitor the silicone thickness. Thus we could not guarantee, as in the simulated experiments, the linearity of the thickness increase. We measured of the silicone layer with a caliper at both ends of the sample in the x-direction. We found 0.4 mm on the left and 1.5 mm on the right with a precision of 0.2 mm. We expected that the thickness variation of the silicone layer would be almost linear between those two values. Since the thicknesses in all the experiments were never greater than 3 mm, we set $a = 0$ mm and $b = 3$ mm as the boundaries for the z_k interval, divided in $P = 90$ samples.

In each experiment, reflection measurements were obtained at our operating frequencies on a regularly spaced grid of 200×80 for the simulated experiments and 526×92 for the real experiment.

Thereafter, we will call 5.2 the method presented in Section 5.2, and 5.3 the method presented in Section 5.3.

6.2 Experiments on simulated data

6.2.1 Noiseless Data

In this experiment, we simulated a noiseless reflection measurement using the modelling explained in Section 4. We thus obtained three reflection maps as shown in Fig.12. To help understanding those maps, we include the central row of each map on Fig.13.

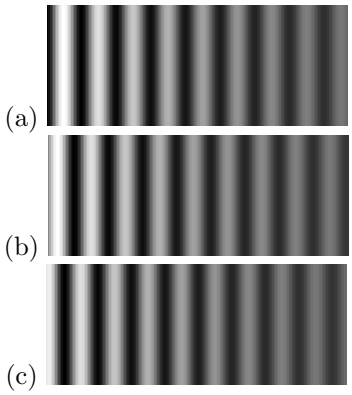

Figure 12: Noiseless far-infrared reflection images of the modelled sample at 279 GHz (a), 284 GHz (b) and 289 GHz (c). The grey-scale values corresponds to the measurement profiles in Fig.13.

The experiment consisted of reconstructing a sampled map of the silicone layer thickness by using method 5.2. The reconstructed map is shown in Fig.14. In this image, the thickness value is represented by a look-up table ranging from green (0 mm) to red (3 mm). As mentioned in Section 5.2, there could be some measurement locations with no thickness estimate. Those locations are shown in dark blue. As can be seen in Fig.14, the thickness values seem to linearly ramp from 0 mm to 3 mm in the x-direction.

To quantify the precision of the reconstruction, we have reported, in Table 1, the absolute mean, maximal values as well as the standard deviation of the reconstruction error. We have also indicated, in the last column, the percentage of locations where a thickness reconstruction was available. Only those locations are used to compute the dispersion indicators of Table 1.

We are interested here in the first row of Table 1 (noiseless data - method 5.2). The reconstruction error was very low in this experiment. The residual error was mostly due to the sampling of the interval $[0, 3]$ mm into $P = 90$ values. Such sampling introduces a theoretical error whose absolute mean is $\frac{1}{4}\frac{3}{90} \approx 0.008$mm. This value is very close to that reported in the second column of Table 1.

Table 1: Reconstruction error

Experiment	Mean	Max	σ	% est.
Noiseless data - 5.2	8.3 μm	16.6 μm	9.62 μm	100.0%
Noisy data - 5.2	78.6 μm	1338.0 μm	164.84 μm	97.2%
Noisy data - 5.3	17.1 μm	391.2 μm	52.15 μm	99.8%

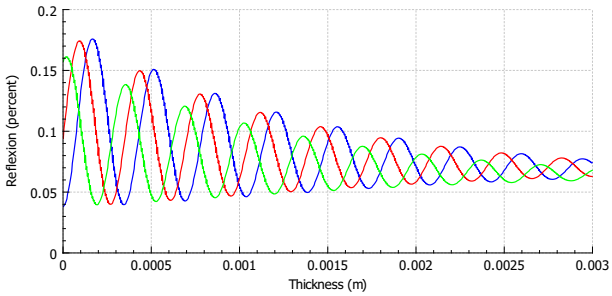

Figure 13: Measurement profiles of the modelled sample reflection response at 279 GHz (blue), 284 GHz (red) and 289 GHz (green).

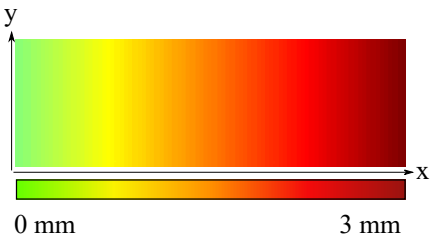

Figure 14: Reconstruction of the noiseless data thickness using method 5.2.

6.2.2 Noisy Data

As mentioned previously, due to measurement noise, method 5.2 can fail in reconstructing the thickness of the silicone layer. We simulated a noisy measurement to highlight this fact and the interest of using method 5.3. In previous experiments, we observed that the spread of the reflection measurement noise distribution was always lower than 0.05. As this distribution was unknown, we applied the principle of insufficient reason to simulate this additive measurement noise by using a centred uniform random variable on $[-0.05, 0.05]$. Naturally, noisy measures are rounded to comply with the fact that the reflection measures remains in $[0, 1]$

As in the previous experiment, we obtained three reflection maps, as shown in Fig.15.

We reconstructed two maps using the two methods 5.2 and 5.3. The map obtained by using method 5.2 is shown in Fig.16, while the map obtained by using method 5.3 is shown in Fig.17,

In Fig.16, the reconstructed map looks like a linear ramp. However, due to noise, a high number of non-reconstructed values (in dark blue) are spread throughout the image. The reconstruction error is quantified in the second row of Table 1. Compared to the previous experiment, the rate of reconstructed thickness values was lower and the reconstruction was less precise.

The third row of Table 1 shows the reconstruction error when using method 5.3. The number of reconstructed thickness values was much higher than with

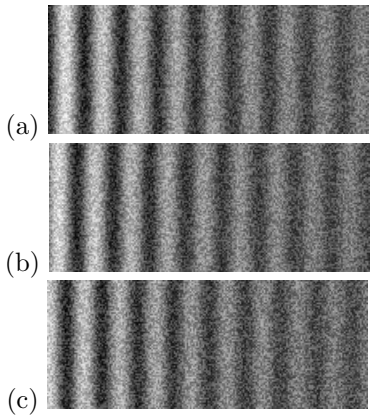

Figure 15: Far-infrared reflection images of the modelled sample at 279 GHz(a), 284 GHz(b) and 289 GHz(c) with noise.

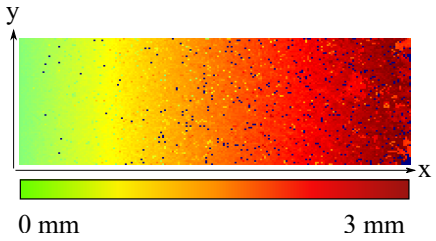

Figure 16: Reconstruction of a noisy data thickness map using method 5.2.

method 5.2 while the reconstruction was more precise. This shows that smoothing the quadratic function leads to a more accurate reconstruction (the mean error is ≈ 4 times lower). Fig.17 shows that mis-reconstructed values are confined to the borders of the map. This may be a border effect of the anisotropic filter.

6.3 Experiments on real data

To carry out this experiment, we used the reflection system described in Section 3 with an optical resolution of 0.15 mm in both directions. As in the simulated experiments, we obtained three measurement maps as shown in Fig.18. Due to the poor control we have on the silicone layer, some unwanted air infiltration can be noted at the right edge of the far-infrared reflection images (a kind of L-shaped measurement artefact).

As in the simulated data experiment, we used both methods 5.2 and 5.3 to reconstruct the thickness map. Since the thickness of the silicone layer could not be fully inspected, we had no ground truth. In order to overcome this lack of ground truth, we achieved a TDS measurement of the thickness of the silicone layer. The analyse of the results we propose was qualitative since we compared

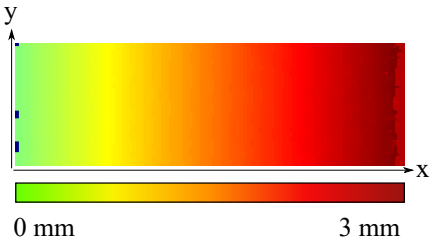

Figure 17: Reconstruction of noisy data's thickness map using method 5.3.

the coherence between the TDS measurement and the reconstructed map.

Fig.19 shows the map obtained by using method 5.2. Within this reconstruction, almost 84% of the values were estimated. We found values ranging from close 0.4 mm on the left to almost 1.5 mm on the right, matching the caliper measurements precision.

Compared to the simulated experiments where non-reconstructed locations were spread throughout the sample, the non-reconstructed locations were clustered. One of those clusters corresponded to the L shaped artefact located at the rightmost part of the images. This was not surprising since the reflection obtained at these sampled locations was not compatible with the modelling we used (the refractive index of the air/silicone mix was not the one we hypothesised).

As in any photon-based measurement system, the measurement noise of the sensor we used is better modelled by a Poisson distribution, i.e. is not stationary in the wide sense (SWS). Therefore, in dark areas where the signal to noise ratio was significantly low, the method we uses - that assumed a SWS of the measurement noise - underperformed the thickness reconstruction at these locations.

We used method 5.3 and obtained the second thickness measurement shown in Fig.20. Method 5.3 reduced the uncertainty in the clustered areas, allowing for reconstruction of more than 99% of the sampled locations. Note that the L-shaped artefact was smoothed to the point of being invisible by the convolution kernel.

The thickness reconstruction was still in accordance with the initial measurements and a transverse cut of that reconstruction is plotted in Fig.21, showing an almost linear progression from approximately 0.4 mm to 1.5 mm. We superimpose on that figure (in blue) a linear ramp from 0.4 mm to 1.5 mm for reference, representing the values that would have been obtained if the silicone thickness increase were linear. The profile obtained by TDS measurement is superimposed in red in Fig.21. This profile confirms the non-linearity of the increase in silicone thickness. The consistency of the reconstructed profile and the TDS measured profile is confirmed by their Pearson correlation coefficient of 0.996.

The thickness variations do not seem to be linear, i.e. note a slight curve on the left half of the profiles. This variation could be expected. The reflection

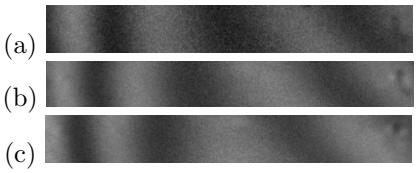

Figure 18: 279 GHz(a), 284 GHz(b) and 289 GHz(c) far-infrared reflection images of our sample.

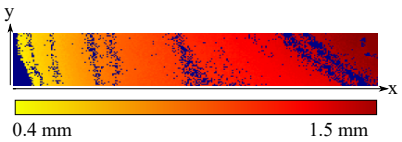

Figure 19: Reconstruction of the real sample thickness with method 5.2.

images in Fig.18 show that the interference patterns are shorter on the left half than on the right half. Shorter interference means a faster phase shift, which in turn means a greater thickness variation. We noted this greater thickness variation on the left half in the TDS profile and in our reconstruction.

7 Conclusion

In this study, we have proposed a fast and convenient method for reconstructing thickness variations of one layer of interest inside a multi layered structure. This method is based on computing the quadratic difference between a limited number of far-infrared reflective responses with modelling based on the known CAD model of the multi layered structure for different possible values of the sought after thickness variation.

The simulation experiments show that the method we propose to invert this ill-posed problem is in line with our modelling of the problem. The experiment with real data tends to confirm the robustness of the method w.r.t. the modelling we chose. Moreover, the reconstructed thickness variation is perfectly consistent with the TDS measurements.

Attentive readers will note that this method strongly relies on the hypothesis that the sample under observation can be locally abstracted as a stack of semi-infinite layers. While this puts severe constraints on the candidate structures for such evaluation, we believe it covers a wide variety of cases. For a more

Figure 20: Reconstruction of the real sample thickness with method 5.3.

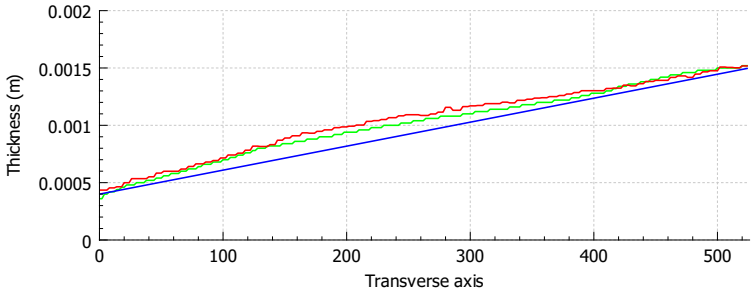

Figure 21: Measurement comparison for the real sample transversal thickness. Our thickness reconstruction (in green). TDS thickness reconstruction (in red). Linear ramp between extreme values (in blue).

geometrically robust approach, the one-dimensional modelling function could be changed to a three-dimensional finite-dimension time-domain simulation, when enough time is available.

While we used a rather inquisitive decision system, a probability-based methodology might efficiently complement our work. In particular, the local minima could be replaced by a non-exclusive analysis, but the computational cost would slow down the entire process, thereby nullifying the main advantages of our study.

References

[1] F. B. Costa, M. A. Machado, G. J. Bonfait, P. Vieira, and T. G. Santos, "Continuous wave terahertz imaging for ndt: Fundamentals and experimental validation," *Measurement*, vol. 172, p. 108904, 2021. [Online]. Available: https://www.sciencedirect.com/science/article/pii/S0263224120313877

[2] Q. Lin, Z. Lin, Y. Li, H. Su, and F. Ma, "Reduce the effects of fabry-perot interference and system dispersion in continuous wave terahertz coherence measurements with two optical-path differences," *Optics and Lasers in Engineering*, vol. 134, p. 106234, 2020. [Online]. Available: https://www.sciencedirect.com/science/article/pii/S014381662030186X

[3] F. Ellrich, M. Bauer, and N. Schreiner, "Terahertz quality inspection for automotive and aviation industries," *J Infrared Milli Terahz Waves 41*, 2020.

[4] N. S. Schreiner, W. Sauer-Greff, R. Urbansky, G. von Freymann, and F. Friederich, "Multilayer thickness measurements below the rayleigh limit using fmcw millimeter and terahertz waves," *Sensors*, vol. 19, no. 18, 2019. [Online]. Available: https://www.mdpi.com/1424-8220/19/18/3910

[5] T. Zwick, J. Haala, and W. Wiesbeck, "A genetic algorithm for the evaluation of material parameters of compound multilayered structures," *IEEE Transactions on Microwave Theory and Techniques*, vol. 50, no. 4, pp. 1180–1187, 2002.

[6] K. Hao, X. Wang, S. Yang, J. Zhang, and Z. Li, "Complex permittivity inversion algorithm with adaptive learning strategy and parameter balancing mechanism," *Optik*, vol. 223, p. 165402, 2020. [Online]. Available: http://www.sciencedirect.com/science/article/pii/S0030402620312389

[7] L. A. C. Fonseca, H. E. Hernandez-Figueroa, G. T. Santos-Souza, and L. L. Bravo-Roger, "Dielectric properties characterization: A simple inverse problem approach," in *2017 IEEE MTT-S International Conference on Numerical Electromagnetic and Multiphysics Modeling and Optimization for RF, Microwave, and Terahertz Applications (NEMO)*, 2017, pp. 22–24.

[8] V. Křesálek and M. Navrátil, "Estimation of complex permittivity using evolutionary algorithm from measured data of reflectance and transmittance in free space," *Microwave and Optical Technology Letters*, vol. 57, no. 7, pp. 1542–1546, 2015. [Online]. Available: https://onlinelibrary.wiley.com/doi/abs/10.1002/mop.29135

[9] D. Junior, D. Braz, C. Silva, and R. Costa-Felix, "Proficiency test on thickness measurement using ultrasound: A metrological aid to improve safety in transportation of dangerous products," *Measurement*, vol. 127, pp. 390–395, 2018.

[10] Z. Zeng, P. Ding, J. Li, S. Jiao, J. Lin, and Y. Dai, "Characteristics of eddy current attenuation and thickness measurement of metallic plate," *Chinese Journal of Mechanical Engineering*, vol. 32, no. 1, pp. 1–9, 2019.

[11] W. Giurlani, E. Berretti, M. Innocenti, and A. Lavacchi, "Coating thickness determination using x-ray fluorescence spectroscopy: monte carlo simulations as an alternative to the use of standards," p. 79, 2019.

[12] A. Chan, J. S. Duker, T. H. Ko, J. G. Fujimoto, and J. S. Schuman, "Normal macular thickness measurements in healthy eyes using stratus optical coherence tomography," pp. 193–198, 2006.

[13] I. Demkovych, H. Petrovska, and Y. Bobitski, "Covering thickness measurement by photothermal method," in *6th International Conference on Laser and Fiber-Optical Networks Modeling, 2004. Proceedings of LFNM 2004.* IEEE, 2004, p. 334.

[14] B. Wang, S. Zhong, T.-L. Lee, K. S. Fancey, and J. Mi, "Non-destructive testing and evaluation of composite materials/structures: A state-of-the-art review," *Advances in Mechanical Engineering*, vol. 12, no. 4, 2020.

[15] J. Jonuscheit, "Terahertz waves for thickness analyses," 2018.

[16] D. Zimdars, J. S. White, G. Stuk, A. Chernovsky, G. Fichter, and S. Williamson, "Large area terahertz imaging and non-destructive evaluation applications," vol. 48, no. 9. The British Institute of Non-Destructive Testing, 2006, pp. 537–539.

[17] Y.-C. Shen and P. F. Taday, "Development and application of terahertz pulsed imaging for nondestructive inspection of pharmaceutical tablet," *IEEE Journal of Selected Topics in Quantum Electronics*, vol. 14, no. 2, pp. 407–415, 2008.

[18] M. Tonouchi, "Cutting-edge terahertz technology," *Nature photonics*, vol. 1, no. 2, pp. 97–105, 2007.

[19] S. Wietzke, C. Jansen, C. Jördens, N. Krumbholz, N. Vieweg, M. Scheller, M. Shakfa, D. Romeike, T. Hochrein, M. Mikulics, and M. Koch, "Industrial applications of thz systems," *Proceedings of SPIE - The International Society for Optical Engineering*, vol. 7385, 07 2009.

[20] I. Duling and D. Zimdars, "Revealing hidden defects," *Nature Photonics volume 3*, 2009.

[21] F. Ospald, W. Zouaghi, R. Beigang, C. Matheis, J. Jonuscheit, B. Recur, J.-P. Guillet, P. Mounaix, W. Vleugels, P. V. Bosom, L. V. Gonzalez, I. Lopez, R. M. Edo, Y. Sternberg, and M. Vandewal, "Aeronautics composite material inspection with a terahertz time-domain spectroscopy system," *Optical Engineering*, vol. 53, no. 3, pp. 1 – 15, 2013. [Online]. Available: https://doi.org/10.1117/1.OE.53.3.031208

[22] M. Triki, A. Duhant, C. Poulin, B. Moulin, C. Archier, T. Antonini, F. Teppe, and W. Knap, "Real-time nondestructive imaging with thz waves," *International Conference on Microwave, Radar and Wireless Communications*, 2016.

[23] F. Schuster, D. Coquillat, H. Videlier, M. Sakowicz, F. Teppe, L. Dussopt, B. Giffard, T. Skotnicki, and W. Knap, "Broadband terahertz imaging with highly sensitive silicon cmos detectors," *Optics express*, vol. 19, no. 8, pp. 7827–7832, 2011.

[24] G. Auton, D. B. But, J. Zhang, E. Hill, D. Coquillat, C. Consejo, P. Nouvel, W. Knap, L. Varani, F. Teppe *et al.*, "Terahertz detection and imaging using graphene ballistic rectifiers," *Nano letters*, vol. 17, no. 11, pp. 7015–7020, 2017.

[25] X. Wang, L. Hou, and Y. Zhang, "Continuous-wave terahertz interferometry with multiwavelength phase unwrapping," *Appl. Opt.*, vol. 49, no. 27, pp. 5095–5102, Sep 2010. [Online]. Available: http://ao.osa.org/abstract.cfm?URI=ao-49-27-5095

[26] S. J. Orfanidis, *Electromagnetic Waves and Antennas*, 1st ed. Rutgers University: www.ece.rutgers.edu/~orfanidi/ewa, 2016.

Appendices

A Mathematics behind the regularisation by connectivity

The regularisation by connectivity we propose is based on the hypothesis that the thickness variation of the layer of interest is continuous, i.e. this function cannot have any sharp changes. This would not be true if this layer were broken, but an assessment of this would be beyond the scope of this study.

The *regularisation by connectivity* we propose involves two steps. First connected sets of local minima of the quadratic function are sought. Second, one optimal set among those sets is selected.

Let $\Omega = [1, N] \times [1, M] \times [1, P] \subset \mathbb{N}^3$. Let us consider the discrete function $E : \Omega \to \mathbb{R}^+$ defined by $E(i, j, k) = Q_{i,j}(z_k)$. Let $\epsilon = \frac{\lambda_1}{4.n_K}$ (with n_K being the known complex refractive index of the LoI) and $\mathcal{V}_\epsilon(k) = \{l = 1 \dots P \ / \ |z_k - z_l| < \epsilon\}$. $V_\epsilon(k)$ represents all the ϵ-neighbourhoods of k, with ϵ being the quarter of the effective wavelength inside the LoI.

The value of $\hat{z}(i, j)$ for each measured location is found by determining the local z-minima of E that are x, y connected. We say that the voxel (i, j, k) is a local z-minimum if $\forall l \in \mathcal{V}_\epsilon(k)$, $E(i, j, k) < E(i, j, l)$. In Fig.7, the red planes represents the sought after local z-minima.

Let $\mathcal{L} \subseteq \Omega$ be the set of all local z-minima of Ω.

The first step of the regularisation procedure consists of finding all subsets of connected voxels of $\mathcal{L}$. We assume that the voxels (i_1, j_1, k_1) and (i_2, j_2, k_2) are connected if $|i_1 - i_2| \leq 1$, $|j_1 - j_2| \leq 1$ and $|z_{k_1} - z_{k_2}| \leq \frac{\epsilon}{2}$.

Let $S_r \subseteq \mathcal{L}$ $(r = 1 \dots R)$ be the R connected subsets of $\mathcal{L}$. Let $\mathcal{C}(S_r) = \frac{1}{|S_r|} \sum_{(i,j,k) \in S_r} E(i, j, k)$ be the mean value of the quadratic error for that connected subset, with $| \bullet |$ being the number of elements of $\bullet$.

The second step of this procedure consists of finding the most probable connected subset, i.e. the set that minimises $\mathcal{C}$: $\hat{S} = \underset{r=1 \dots R}{\arg\min} \{\mathcal{C}(S_r)\}$. If the LoI thickness variation is regular enough, then for any (i, j) couple there is at most one value k such that $(i, j, k) \in \hat{S}$.

We thus can assign the thickness reconstruction as follows:
for each $(i, j, k) \in \hat{S}$, $\hat{z}(i, j) = z_k$.

At this stage, there can be some measurement locations with no thickness estimate. This occurs when the reflection measurements are affected by noise that is strong enough to offset the z_k array by more than $\frac{\epsilon}{2}$. In that case, we can seek the next minimum of $\mathcal{C}$ or interpolate the current solution.